ORIGINAL ARTICLE

FFEMS Fatigue & Fracture of Engineering Materials & Structures   WILEY

Cracking of a functionally graded coating due to sliding contact with heat generation

Mehmet N. Balci[1] ⓘ | **Serkan Dag**[2] | **Bora Yildirim**[1]

[1]Mechanical Engineering Department, Hacettepe University, Ankara, Turkey

[2]Mechanical Engineering Department, Middle East Technical University, Ankara, Turkey

Correspondence
Mehmet N. Balci, Mechanical Engineering Department, Hacettepe University, 06800 Ankara, Turkey.
Email: mehmetbalci@hacettepe.edu.tr

Abstract
In this work, the thermal contact problem of a rigid flat punch sliding over functionally graded material (FGM) coating with a surface crack is investigated. The surface of a homogeneous isotropic substrate is ideally coated by FGM. The coefficient of friction on the contact surface is assumed to be constant, and dry Coulomb friction law is applied. The major purpose of this study is to compute the stress intensity factors at the tip of a surface crack under thermomechanical loading. In this perspective, the thermoelastic contact and the surface crack problems are modeled using finite element method. An iterative solution procedure based on finite elements is developed to solve the contact/crack problem until generated frictional heat reach the steady-state condition. Obtained results are compared to those available in the open literature, and a good agreement is observed. Presented results involve stress intensity factors computed under various thermoelastic sliding conditions.

KEYWORDS
contact mechanics, FGM coating, finite element method, frictional heat generation, surface crack

Highlights
- A surface crack problem in an FGM coating subjected to sliding contact is examined.
- Frictional heat due to punch has a remarkable influence on stress intensity factors.
- The iterative computational method is developed to determine stress intensity factors.
- Frictional heat and material properties significantly affect stress intensity factors.

1 | INTRODUCTION

Functionally graded materials (FGMs) are a nonconventional type of composites, which have functional alteration in the volume fractions of the ingredient phases. In tribological applications, functionally graded coatings provide significant advantages over conventional ceramic coatings. One of the most important benefits is the alleviation of thermomechanical mismatch between a coating and a substrate. Hence, behavior of FGMs under mechanical and thermal loading conditions is examined in quite a large number of research studies. Additionally, both experimental and computational works are conducted to develop methods of solution for contact mechanics analysis of functionally graded components. The focus of conducted research is usually on determining whether FGM coatings resist contact-related damage such as cracking and wear under severe environments including heat and corrosion. It has been proven that FGMs improve the tribological performance.

Solutions to various types of contact problems for homogeneous materials are available in monographs on contact mechanics.[1,2] Hills and Sackfield[3] presented a solution for dissimilar elastic cylinders subjected to sliding contact. The articles on contact mechanics of FGMs examine the influences of a number of factors including property variation profile, punch profile and speed, coefficient of friction, and coating thickness. Giannakopoulos and Suresh[4,5] investigated the axisymmetric problems of a graded half-space loaded by various types of indenters. The elastic modulus is expressed by a power function. Giannakopoulos and Pallot[6] developed closed-form solutions for the problem of a functionally graded substrate loaded by a rigid stamp. Suresh et al[7] examined the indentation problem of graded materials by spherical indenters using analytical and experimental methods. Guler and Erdogan[8–10] studied contact mechanics of an FGM coating bonded to a homogeneous isotropic substrate and utilized different rigid stamp profiles. Apatay et al[11] calculated subsurface stresses in graded coatings subjected to rigid flat punch contact. Contact mechanics problem between a laterally graded elastic medium and a sliding rigid punch was studied by Dag et al.[12] Both analytical and computational methods were proposed, and effects of the lateral non-homogeneity and the surface friction characteristics upon contact stresses were examined. Ke and Wang[13,14] investigated the contact problem for an FGM coating with an arbitrary spatial variation in the shear modulus. They discretized the graded coating by a finite number of layers and adopted the transfer matrix approach. In addition, Dag[15] considered spatial variation of the coefficient of friction in contact mechanics analysis of laterally graded materials. El-Borgi et al[16,17] developed analytical

solutions to frictionless receding contact problem between a graded layer and a homogeneous semi-infinite substrate. Choi and Paulino[18] examined interfacial cracking in a graded coating/substrate system under the effect of frictional stamp. Dag et al[19] studied surface cracking of FGM coating under contact-type loading. Talezadehlari et al[20] developed a computational method based on finite differences for the coupled contact/crack problems of a graded coating and a homogeneous substrate system.

Fracture mechanics problems of FGMs have also been considered in various studies to quantify the impact of material gradation on crack tip parameters. A solution to a semi-infinite crack in isotropic FGMs was obtained by Gu and Asaro,[21] and it was indicated that the material gradients had a strong influence on the stress intensity factors (SIFs). Jin and Batra[22] provided SIFs for ZrO_2-Ti FGM with an edge crack under various loading cases. Dolbow and Gosz[23] developed an interaction energy integral for determination of SIFs for FGMs in a mixed-mode case. Dag and Erdogan[24] studied surface cracking of an FGM under general loading conditions. A coupled type crack and contact problem for functionally graded half-plane involving a surface crack was solved by Dag and Erdogan.[25] El-Borgi et al[26] analyzed the surface crack problem in a graded coating/substrate system. The main purpose of that study was to investigate the influence of coating layer thickness and non-homogeneity parameter on the crack tip SIFs in a mixed-mode. Guo et al[27] carried out research on mode-(1) fracture problem for a functionally graded orthotropic strip. Dag and Ilhan[28] developed computational and analytical techniques for mixed-mode fracture analysis of a functionally graded orthotropic material (FGOM). Dag et al[29] investigated mixed-mode fracture mechanics problems of FGOM under both mechanical and thermal loads. Thermal fracture analysis of FGMs was conducted by Dag[30] via equivalent domain integral (EDI) approach, and SIFs for various thermal conditions were presented. Yildirim[31] studied thermal shock fracture for functionally graded layer with an edge crack using the finite element method (FEM).

In frictional sliding contact problems, considerable level of heat can be generated due to friction, and this in turn may impact distribution of contact pressure and thermomechanical response of the structure. This type of thermoelastic contact problems involves heat source effect due to the friction force. Barber[32] presented solutions for steady-state thermoelastic contact problems in which frictional heat due to sliding is generated between two semi-infinite solids. Steady-state motion of an insulated rigid flat ended punch on a thermally conducting half-space was examined by Hills and Barber.[33] The thermoelastic contact problem between a cooled punch and a homogeneous isotropic half-plane was examined by Barber.[34] Steady-state

solutions were developed by applying the concept of thermal contact resistance, which varied inversely with the contact pressure. Yevtushenko and Kulchytsky-Zyhailo[35] detailed an approximate solution for the thermoelastic contact problem involving a nonconducting half-space and an elastic punch. Kulchytsky-Zyhailo[36] put forward a simplified solution for the three-dimensional (3D) contact problem involving heat generation. Thermoelastic contact between a sliding frictional flat stamp and a coating–FGM interlayer and a homogeneous substrate system was considered by Choi and Paulino,[37] and distributions of contact stresses were computed for different geometry and loading conditions. Liu et al[38] investigated contact mechanics of FGMs by considering frictional heating. Chen and Chen[39] examined thermomechanical behavior of a finite graded layer under contact load. They presented numerical results regarding contact stress and temperature distributions caused by rigid flat and cylindrical punches. Balci et al[40] analyzed the sliding frictional contact problem for a rigid flat punch and a homogeneous substrate by means of FEM. Frictional heat generation and temperature-dependent properties are accounted for in the proposed methodology. Frictional heat generation accounted for temperature-dependent material properties. Finite element analysis of subsurface stresses in FGMs under frictional contact with heat generation is presented in Balci et al.[41]

A detailed investigation of the literature as described above indicates that there is no work on surface fracture of graded coatings under contact loading involving frictional heat generation. Dag et al[19] examined surface cracking under contact loading, but frictional heat generation and its effects were not accounted for. The main objective in the present study is to perform fracture analysis of an FGM coating subjected to contact loading involving *frictional heat generation*.

Steady-state response of the thermoelastic contact is investigated under the assumption that the punch sliding speed is sufficiently small. This assumption implies that convective effects are not as influential as the conductive effects. The convective and inertia terms are, respectively, ignored in the heat equation and Navier equations as also previously done in other studies.[37,40,41] Thus, the present study investigates steady-state thermoelastic contact/crack problem between an FGM coating and a rigid flat punch.

2 | PROBLEM DEFINITION AND BOUNDARY CONDITIONS

The schematic of the problem examined is depicted in Figure 1. We consider an FGM coating of thickness h, which contains a surface crack of length d and is ideally
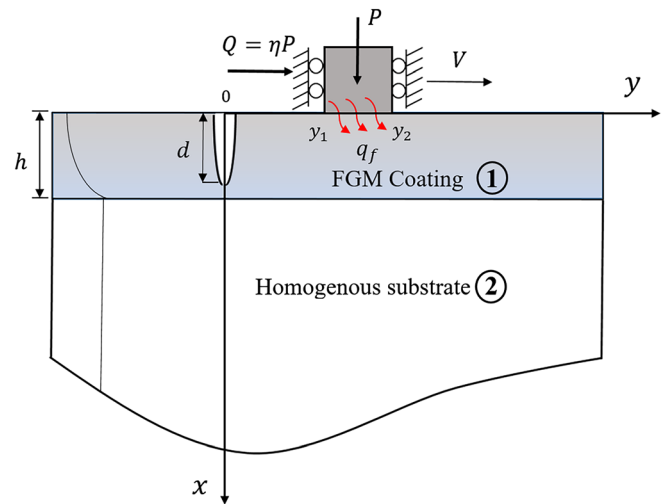

FIGURE 1 A crack emerging on the surface of FGM coating in contact with a sliding punch generating frictional heat. [Colour figure can be viewed at wileyonlinelibrary.com]

bonded to an isotropic homogeneous substrate. The coating is exposed to a frictional sliding contact with a rigid flat punch, which slides over the surface of the coating with a relatively small velocity V. Frictional shear stress induced in the contact region is assumed to cause heat generation. Furthermore, the punch is thermally nonconductive, and the heat flows into the FGM coating. The coordinates of the contact zone extends from $y = y_1$ to $y = y_2$. The transferred normal and lateral loads are, respectively, represented by P and Q. Coulomb's friction law is valid, and thus, $Q = \eta P$, where η is kinetic friction coefficient. The free surface outside the contact zone and crack surfaces are considered thermally insulated. Since P is presumed sufficiently small, inertial effects are neglected. The coated medium is in a state of either plane stress or strain. The concurrent effects resulting from punch loading and heat generation induce mode-(1) and mode-(2) SIFs at the tip of the surface crack. Crack length d is less than or equal to coating thickness h, and the crack tip lies either in the coating or at the interface.

For both mediums of coating and the substrate, planar constitutive relations of thermoelasticity read

$$\sigma_{jxx} = \frac{\mu_j}{\kappa_j - 1}\left[\left(1 + \kappa_j\right)\frac{\partial u_j}{\partial x} + \left(3 - \kappa_j\right)\frac{\partial v_j}{\partial y} - 4\overline{\alpha}_j \Delta T_j\right], j = 1, 2,$$

(1)

$$\sigma_{jyy} = \frac{\mu_j}{\kappa_j - 1}\left[\left(3 - \kappa_j\right)\frac{\partial u_j}{\partial x} + \left(1 + \kappa_j\right)\frac{\partial v_j}{\partial y} - 4\overline{\alpha}_j \Delta T_j\right], j = 1, 2,$$

(2)

$$\sigma_{jxy} = \mu_j\left(\frac{\partial u_j}{\partial y} + \frac{\partial v_j}{\partial x}\right), j = 1,2, \tag{3}$$

$$\kappa_j = \begin{cases} 3 - 4\nu_j, & \text{plane strain,} \\ \dfrac{3 - \nu_j}{1 + \nu_j}, & \text{plane stress,} \end{cases} \tag{4}$$

$$\overline{\alpha}_j = \begin{cases} (1 + \nu)\alpha_j, & \text{plane strain,} \\ \alpha_j, & \text{plane stress,} \end{cases} \tag{5}$$

where σ is stress; u and v are displacement components in x- and y-directions; T is temperature; and μ, κ, ν, and α are, respectively, shear modulus, Kolosov's parameter, Poisson's ratio, and thermal expansion coefficient. The subscript, j, is equal to 1 for the FGM coating and 2 for the homogeneous substrate. Previous studies show that the effect of the variation in the Poisson's ratio on the mechanical behavior is not at a significant level.[19,24,25] For this reason, Poisson's ratios of the FGM coating and the substrate are assumed to be constant and equal.

The temperature distribution in the coating–substrate system is governed by the heat equation, which is expressed as follows for the FGM coating:

$$k_1\left(\frac{\partial^2 T_1}{\partial x^2} + \frac{\partial^2 T_1}{\partial y^2}\right) + \frac{\partial k_1}{\partial x}\frac{\partial T_1}{\partial x} = 0. \tag{6}$$

Governing partial differential equations of thermoelasticity for the FGM coating are derived by substituting Equations (1)–(3) into equations of equilibrium and expressed in the form

$$\begin{aligned}
&\frac{\kappa_1 + 1}{\kappa_1 - 1}\mu_1\frac{\partial^2 u_1}{\partial x^2} + \mu_1\frac{\partial^2 u_1}{\partial y^2} + \frac{2\mu_1}{\kappa_1 - 1}\frac{\partial^2 v_1}{\partial x \partial y} \\
&+ \frac{\kappa_1 + 1}{\kappa_1 - 1}\frac{\partial \mu_1}{\partial x}\frac{\partial u_1}{\partial x} + \frac{3 - \kappa_1}{\kappa_1 - 1}\frac{\partial \mu_1}{\partial x}\frac{\partial v_1}{\partial x} \\
&= \left(\frac{4\mu_1}{\kappa_1 - 1}\frac{\partial \overline{\alpha_1}}{\partial x} + \frac{4\overline{\alpha_1}}{\kappa_1 - 1}\frac{\partial \mu_1}{\partial x}\right)\Delta T_1 \\
&+ \frac{4\mu_1}{\kappa_1 - 1}\overline{\alpha_1}\frac{\partial \Delta T_1}{\partial x},
\end{aligned} \tag{7}$$

$$\begin{aligned}
&\mu_1\frac{\partial^2 v_1}{\partial x^2} + \frac{\kappa_1 + 1}{\kappa_1 - 1}\mu_1\frac{\partial^2 v_1}{\partial y^2} + \mu_1\frac{\partial^2 u_1}{\partial x \partial y} + \frac{3 - \kappa_1}{\kappa_1 - 1}\mu_1\frac{\partial^2 u_1}{\partial x \partial y} \\
&+ \frac{\partial \mu_1}{\partial x}\frac{\partial u_1}{\partial y} + \frac{\partial \mu_1}{\partial x}\frac{\partial v_1}{\partial x} \\
&= \frac{4\overline{\alpha_1}\mu_1}{\kappa_1 - 1}\Delta T_1,
\end{aligned} \tag{8}$$

The governing partial differential equations (PDEs) of the homogeneous substrate can be obtained by equating the material property derivatives to zero.

The contact/crack problem illustrated in Figure 1 has to be solved by considering the thermal and mechanical boundary conditions. Since the rigid flat punch is nonconductive, the heat generated due to friction in the contact zone directly flows into the FGM coating without any loss to the surroundings. Then, in the contact zone, the condition

$$k_1(0)\frac{\partial T(0,y)}{\partial x} = \begin{cases} -q_f(y), & y_1 < y < y_2 \\ 0, & \text{otherwise} \end{cases} \tag{9}$$

has to be satisfied. The term q_f is the heat flux in the contact region and expressed as

$$q_f(y) = -V\sigma_{xy}(0,y), \; y_1 < y < y_2. \tag{10}$$

Continuity conditions at the interface require that

$$T_1(h,y) = T_2(h,y), \; \frac{\partial T_1}{\partial x}(h,y) = \frac{\partial T_2}{\partial x}(h,y), \; -\infty < y < \infty. \tag{11}$$

The condition

$$\frac{\partial T_1(x,0^-)}{\partial y} = \frac{\partial T_1(x,0^+)}{\partial y} = 0, \; 0 < x < d, \tag{12}$$

ensures that thermally insulated faces are valid for the edge crack. Outside the crack region, both the temperature and the heat flux should be continuous, which implies

$$T_j(x,0^-) = T_j(x,0^+), \frac{\partial T_j(x,0^-)}{\partial y} = \frac{\partial T(x,0^+)}{\partial y}, j = 1,2, x > d. \tag{13}$$

For the coupled crack and contact problem, mechanical boundary conditions at the surface and interface are

$$\sigma_{xx}(0,y) = \sigma_{xy}(0,y) = 0, \; -\infty < y < y_1, y_2 < y < \infty. \tag{14}$$

$$\sigma_{xx}(0,y) = \sigma(y), \sigma_{xy}(0,y) = \tau(y) = \eta\sigma(y), y_1 < y < y_2, \tag{15}$$

$$u_1(h,y) = u_2(h,y), v_1(h,y) = v_2(h,y), \; -\infty < y < \infty, \tag{16}$$

$$\sigma_{1xx}(h,y) = \sigma_{2xx}(h,y), \sigma_{2xy}(h,y) = \sigma_{2xy}(h,y), -\infty < y < \infty. \quad (17)$$

Since the punch is rigid and flat, x-component of displacement in the contact region, $u(0,y)$, is constant. Thus, displacement derivative condition can be given as

$$\frac{\partial}{\partial y} u(0,y) = 0, y_1 < y < y_2. \quad (18)$$

For a fully open crack, the crack surfaces are traction-free, and the corresponding free-surface conditions are[*]

$$\sigma_{yy}(x,0^-) = \sigma_{yy}(x,0^+) = 0, \ 0 < x < d, \quad (19)$$

$$\sigma_{yy}(x,0^-) = \sigma_{yy}(x,0^+) = 0, \ 0 < x < d. \quad (20)$$

Lastly, the equilibrium of the rigid punch requires that

$$\int_{y_1}^{y_2} \sigma_{xx}(0,y) \, dy = -P. \quad (21)$$

3 | FINITE ELEMENT MODELING AND ANALYSIS

The problem definition described in Section 2 consists of couplings between thermal and mechanical problems and crack and contact problems. The coupled problems defined are solved by the FEM. The developed finite element solution procedures are integrated into ANSYS[42]—the general-purpose finite element analysis software. Both the FGM coating and the homogeneous substrate are discretized by the triangular counterparts of the quadrilateral elements, PLANE 77 and PLANE 183, which are used in thermal and mechanical analyses, respectively. The triangular element is generated by merging the three nodes of the corresponding quadrilateral element as

---

[*]Note that a crack under contact loading could be fully open, partially open, or completely closed depending upon the values of the large number of parameters affecting the solution. For a crack under closure, the mode-1 stress intensity factor becomes negative. However, the negative result will still be useful if it is employed in a superposition scheme for a combined loading that leads to a positive resultant mode-1 stress intensity factor. Previous studies regarding purely mechanical contact loading show that the edge crack is fully open for relatively larger values of the friction coefficient.[25,53]

depicted in Figure 2. The square-root singularity that exists at the tip of the surface crack is simulated by utilizing quarter-point singular elements around the crack tip. The geometry of a singular element is provided in Figure 2C. Moreover, Figure 2D depicts all elements in the isoparametric coordinate system.

The finite element model developed is shown in Figure 3. In contact mechanics analysis, the rigid punch is modeled by contact line elements TARGE169, whereas the deformable contact surface is discretized by CONTA172. In total, 300 CONTA172 and 2 TARGE169 elements are used in the computations. The mesh density is refined especially in the contact region and around the crack tip to be able to calculate contact stresses and SIFs with a high degree of accuracy. The dimensions in the finite element model are denoted by $(y_2 - y_1)$, L_1, L_2, and h, which correspond to punch width, substrate width, substrate height, and coating thickness, respectively. The dimensions L_1 and L_2 are specified much larger than the size of contact zone to be able to eliminate boundary effect and generate the computational results for a half-plane. The ratios $(y_2 - y_1)/L_1$ and L_2/L_1 are, respectively, specified as 1/70 and 6/7. The continuous change in the properties within the FGM coating is modeled by calculating the thermomechanical properties of each finite element in accordance with its centroidal coordinates. Each finite element is therefore homogeneous; however, the property variations from element to element follow the power function definitions provided by Equations (1)–(3). This is the so-called homogeneous element approach, which was previously shown to lead to highly accurate results in both contact and fracture mechanics analyses.[12,43] Contact mechanics simulations are conducted by applying the augmented Lagrange method. This technique is based on the total potential energy theorem and known to lead to more accurate results compared to those computed by Penalty, Lagrange, and Lagrangian multiplier methods.[44,45]

The coupled crack and contact problem defined requires thermal and mechanical analyses. Heat flux that flows into the composite medium however depends on the shear stress as conveyed by Equation (10). Because of this nonlinear behavior, an iterative solution procedure is proposed to compute contact stresses and SIFs. The first computation is carried out for a moving punch without heat generation. Resulting shear stress is utilized to calculate heat flux and temperature distribution. Computed temperature distribution is then applied in the next mechanical analysis. These iterations are performed until convergence is achieved. The implemented algorithm checks the nodal values of heat flux at the contact nodes and stops the procedure when the approximate errors fall below a predefined percent tolerance. The general steps of
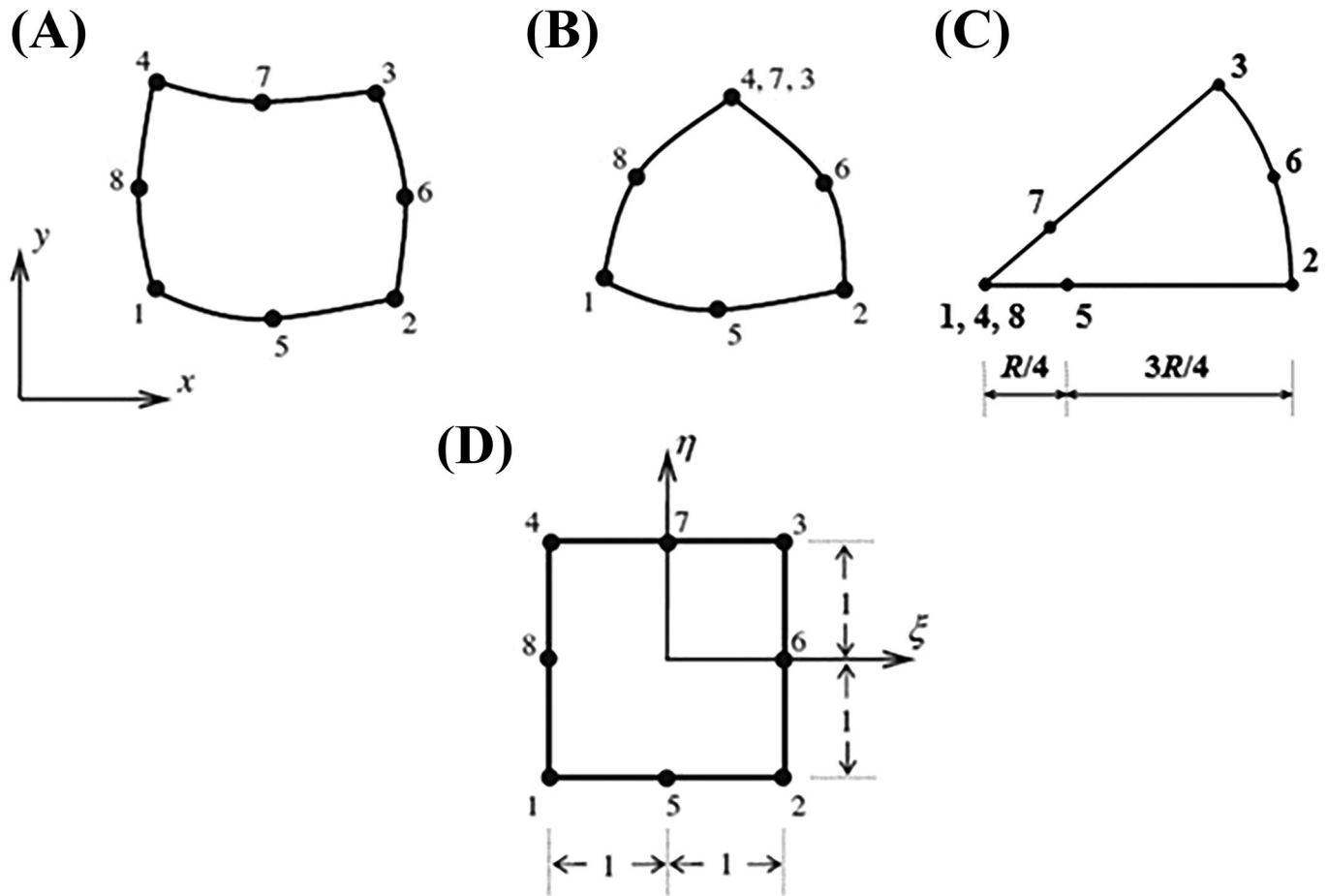
FIGURE 2 (A) PLANE 183/PLANE 77 element. (B) Its triangular counterpart. (C) Singular quarter-point element. (D) Finite elements in the local (ξ,η) coordinate system.

the algorithm developed to compute contact stresses and mode-(1) and mode-(2) SIFs are provided in Figure 4.

Once the converged contact mechanics solution is obtained, the SIFs can be calculated. In this study, we implemented the displacement correlation technique (DCT) for the computation of the SIFs.[28,46–49] The method is applied by utilizing the quarter-point singular elements depicted in Figure 5. The circular region, $r \leq R$, around the crack tip is modeled by means of these elements. The quarter-point element is formed using the eight-noded quadrilateral element shown in Figure 2. Three nodes of the quadrilateral element are merged at the crack tip. The midpoint nodes on the sides are relocated to the quarter points at $r = R/4$. The wedge-shaped elements generated display the square-root singularity in the strain field and have a bounded stiffness matrix.

Displacement fields for the quarter-point elements in the isoparametric coordinate system shown in Figure 2 are given by Dag and Ilhan[28]:

$$u(\xi,\eta) = \sum_{i=1}^{8} N_i(\xi,\eta) u_i, \qquad (22)$$

$$v(\xi,\eta) = \sum_{i=1}^{8} N_i(\xi,\eta) v_i, \qquad (23)$$

where u_i and v_i are nodal displacements and $N_i(\xi,\eta)$ are shape functions, which are of the forms

$$
\begin{aligned}
N_i(\xi,\eta) = &\left[(1+\xi\xi_i)(1+\eta\eta_i) - (1-\xi^2)(1+\eta\eta_i) \right. \\
&\left. - (1-\eta^2)(1+\xi\xi_i)\right]\frac{\xi_i^2\eta_i^2}{4} \\
&+ (1-\xi^2)(1+\eta\eta_i)(1-\xi_i^2)\frac{\eta_i^2}{2} \\
&+ (1-\eta^2)(1+\xi\xi_i)(1-\eta_i^2)\frac{\xi_i^2}{2}, \\
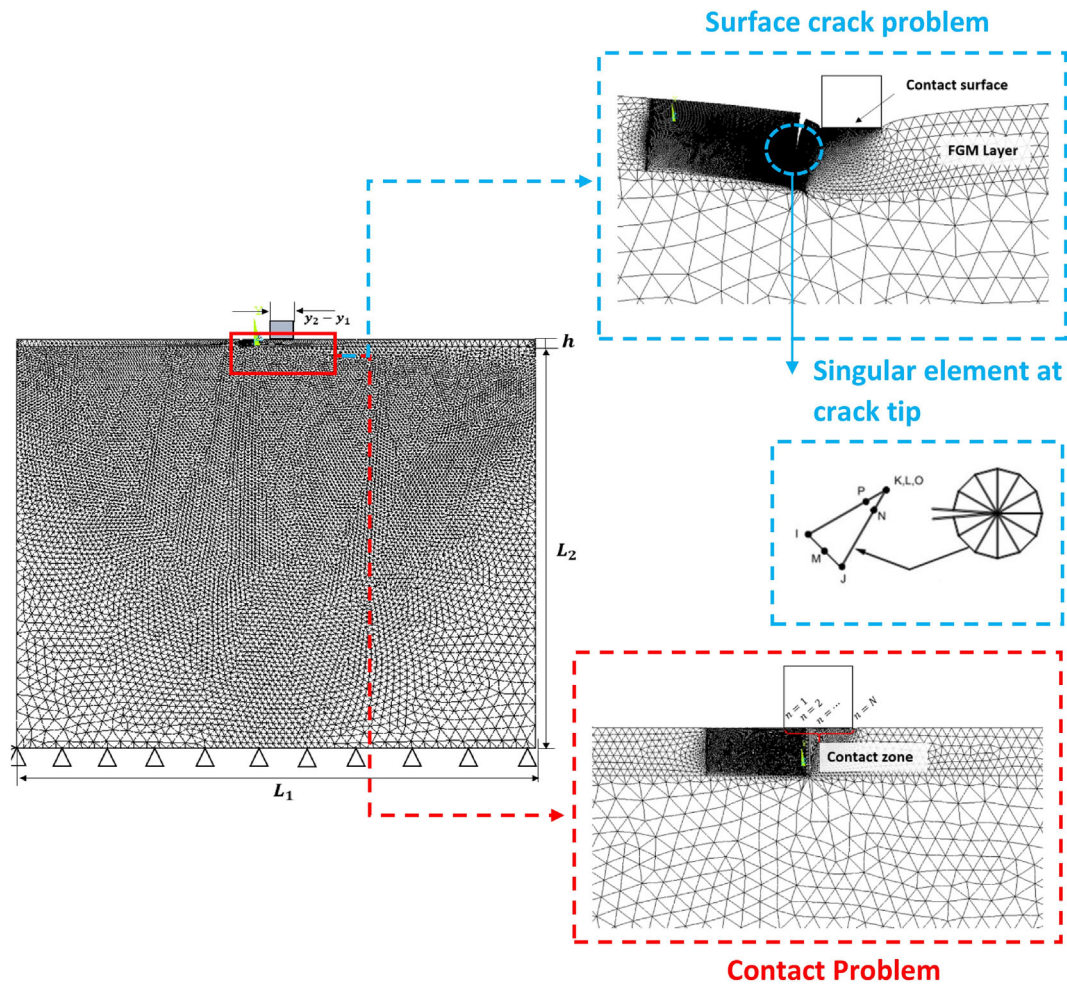i = &1,...,8.
\end{aligned}
\qquad (24)
$$

FIGURE 3 FEM model for the contact/crack problem and close-up views around contact and crack zones. [Colour figure can be viewed at wileyonlinelibrary.com]

In the DCT, the asymptotic displacement fields are correlated with the displacement fields of the quarter-point elements located on the crack faces. Asymptotic distributions of the displacement components at the tip of the edge crack in the polar coordinate system (r,θ) shown in Figure 4 are expressed as follows[49,50]:

$$u(r,\theta) = \frac{K_I}{2\mu^{\text{tip}}}\sqrt{\frac{r}{2\pi}}\cos\left(\frac{\theta}{2}\right)\left\{\kappa^{\text{tip}} - 1 + 2\sin^2\left(\frac{\theta}{2}\right)\right\} + \frac{K_{II}}{2\mu^{\text{tip}}}\sqrt{\frac{r}{2\pi}}\sin\left(\frac{\theta}{2}\right)\left\{\kappa^{\text{tip}} + 1 + 2\cos^2\left(\frac{\theta}{2}\right)\right\},$$
(25)

$$v(r,\theta) = \frac{K_I}{2\mu^{\text{tip}}}\sqrt{\frac{r}{2\pi}}\sin\left(\frac{\theta}{2}\right)\left\{\kappa^{\text{tip}} + 1 - 2\cos^2\left(\frac{\theta}{2}\right)\right\} - \frac{K_{II}}{2\mu^{\text{tip}}}\sqrt{\frac{r}{2\pi}}\cos\left(\frac{\theta}{2}\right)\left\{\kappa^{\text{tip}} - 1 - 2\sin^2\left(\frac{\theta}{2}\right)\right\},$$
(26)

where K_I and K_{II} are, respectively, mode-(1) and mode-(2) SIFs and the superscript "tip" implies that the corresponding material property has to be computed at the crack tip. The asymptotic fields given by these expressions are exactly same as those valid for a crack positioned in a homogeneous medium. The material properties in a continuously graded medium however are variable, and their crack-tip values are to be used in the asymptotic fields.

From Equations (25) and (26), crack opening displacements are obtained as

$$v(r,\pi) - v(r,-\pi) = \frac{\kappa + 1}{\mu}\sqrt{\frac{r}{2\pi}}K_I, \quad u(r,\pi) - u(r,-\pi)$$
$$= \frac{\kappa + 1}{\mu}\sqrt{\frac{r}{2\pi}}K_{II}.$$
(27)

The crack opening displacements for the quarter-point elements shown in Figure 5 are of the forms[51]

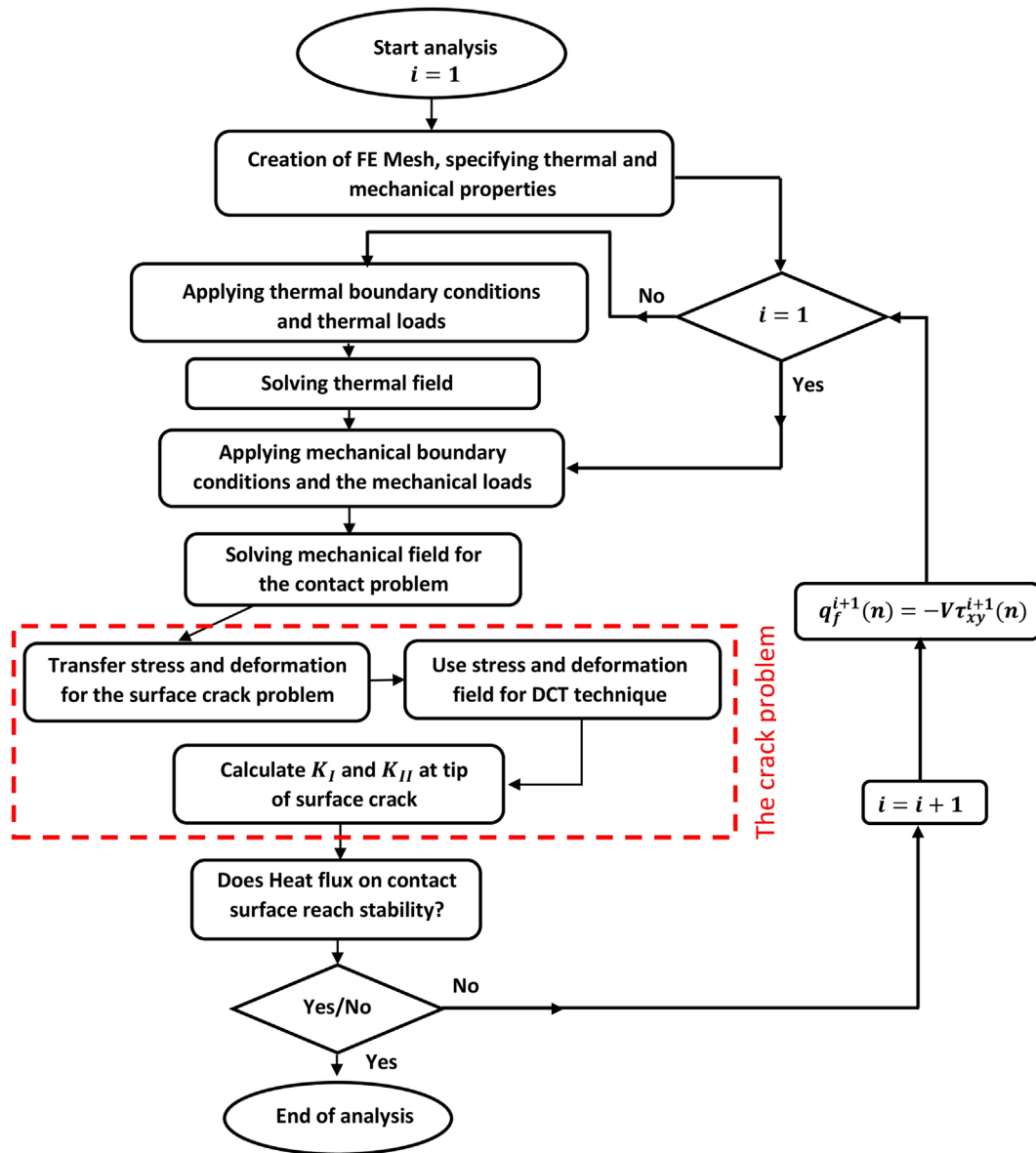**FIGURE 4** Developed algorithm to solve thermoelastic contact and a surface crack problem. [Colour figure can be viewed at wileyonlinelibrary.com]

$$v(r,\pi) - v(r,-\pi) = \{4(v_E - v_C) - (v_D - v_B)\}\sqrt{\frac{r}{R}}, \quad (28)$$

$$u(r,\pi) - u(r,-\pi) = \{4(u_E - u_C) - (u_D - u_B)\}\sqrt{\frac{r}{\pi}}. \quad (29)$$

Equating the respective expressions, K_I and K_{II} are found as

$$K_I = \frac{\mu^{tip}}{\kappa^{tip}+1}\sqrt{\frac{2\pi}{R}}\{4(v_E - v_C) - (v_D - v_B)\}, \quad (30)$$

$$K_{II} = \frac{\mu^{tip}}{\kappa^{tip}+1}\sqrt{\frac{2\pi}{R}}\{4(u_E - u_C) - (u_D - u_B)\}. \quad (31)$$

4 | NUMERICAL RESULTS

4.1 | Convergence analysis

Convergence studies are carried out in order to determine the number of elements to be used in modeling. Exponential expressions are considered to simulate the continuous functional variations of the thermomechanical properties in the FGM coating. Properties are expressed as follows:

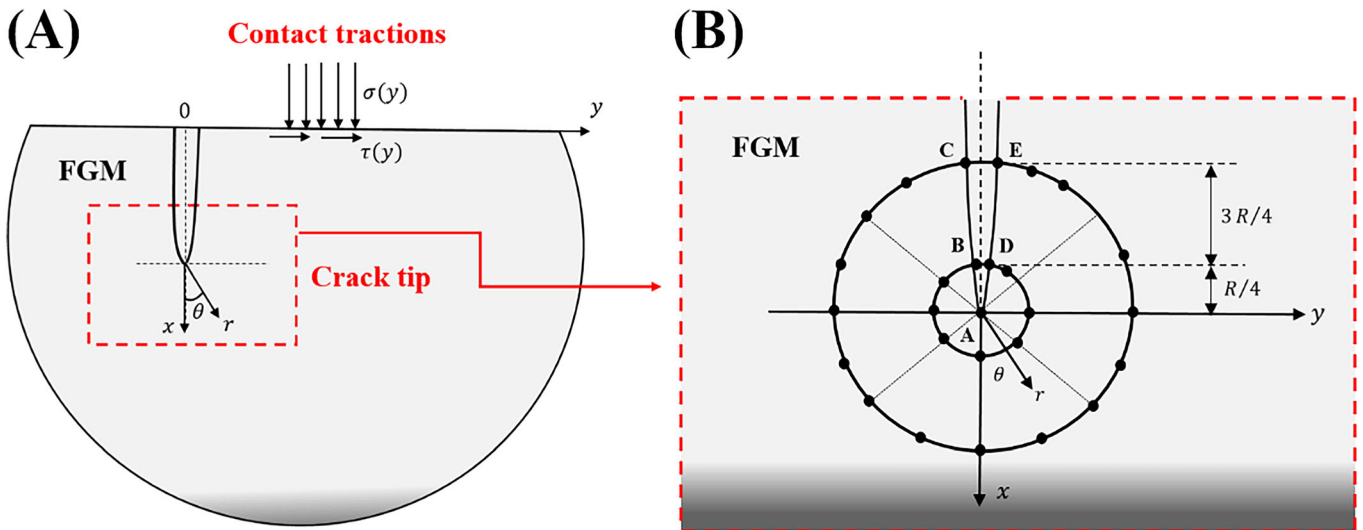$$\mu_1(x) = \mu_1^0 \exp(\beta_1 x), \ 0 \leq x \leq h, \quad (32)$$

FIGURE 5 (A) The Cartesian (x,y) and polar (r,θ) coordinate systems around the crack tip. (b) The quarter-point singular element at the crack tip in FGM medium. [Colour figure can be viewed at wileyonlinelibrary.com]

$$k_1(x) = k_1^0 \exp(\beta_2 x), \tag{33}$$

$$\alpha_1(x) = \alpha_1^0 \exp(\beta_3 x), \; 0 \leq x \leq h, \tag{34}$$

$$\mu_2(x) = \mu_1^h, \;\; x \geq h, \tag{35}$$

$$k_2(x) = k_1^h, \;\; x \geq h, \tag{36}$$

$$\alpha_2(x) = \alpha_1^h, \;\; x \geq h, \tag{37}$$

$$\beta_1 = \frac{1}{h} \ln\left(\frac{\mu_1^h}{\mu_1^0}\right), \; \beta_2 = \frac{1}{h} \ln\left(\frac{k_1^h}{k_1^0}\right), \; \beta_3 = \frac{1}{h} \ln\left(\frac{\alpha_1^h}{\alpha_1^0}\right), \tag{38}$$

where the exponents, β_i, are non-homogeneity constants and their definitions by Equation (38) imply that the properties are continuous at the interface, $x = h$. The coating is assumed to be 100% zirconia (ZrO_2) at $x = 0$ and 100% titanium alloy Ti-6Al-4V at $x = h$. Properties of these constituent phases are tabulated in Table 1. Poisson's ratio in the coating and substrate materials are equal to 0.3. Four different mesh configurations are considered in convergence studies, and the total numbers of finite elements corresponding to each case are given as 43,478 for Case 1, 55,710 for Case 2, 122,086 for Case 3, and 154,446 for Case 4. The lowest and highest numbers of elements are, respectively, applied in Cases 1 and 4.

The dimensionless SIFs

TABLE 1 Material properties of the constituent phases.[52]

Material property	ZrO_2	Ti-6Al-4V
Thermal conductivity, k_1^0, k_1^h	2.036 W $(mK)^{-1}$	18.1 W $(mK)^{-1}$
Elastic modulus, E_1^0, E_1^h	117.0 GPa	66.2 GPa
Thermal expansion coefficient α_1^0, α_1^h	$7.11(10)^{-6} \; K^{-1}$	$10.3(10)^{-6} \; K^{-1}$

$$K_{In} = \frac{\sqrt{d}}{P} K_I, \; K_{IIn} = \frac{\sqrt{d}}{P} K_{II}, \tag{39}$$

are evaluated in the convergence computations. The normalized punch speed definition

$$V_0 = \frac{\mu_1^0 (1+\nu) \alpha_1^0 (y_2 - y_1)\eta}{2 k_1^0 (\kappa + 1)} V, \tag{40}$$

given in Choi and Paulino[37] is adopted and used to specify the punch speed.

Tables 2 and 3 present dimensionless SIFs generated for the four cases mentioned. The results given in Tables 2 and 3 are calculated for punch speed $V_0 = 0.05$. In all cases crack length is $d/h = 0.8$. The SIFs and percent errors are presented for nine different values of dimensionless punch end-point coordinate y_1/d. Since largest number of elements is considered in Case 4, percent approximate errors for mode-(1) and mode-(2) SIFs are

TABLE 2 Normalized mode-(1) SIF results and relative errors $V_0 = 0.05$, $d/h = 0.8$, $\eta = 0.3$, $\beta_1 = -0.0569$, $\beta_2 = 0.218$, $\beta_3 = 0.0371$, $(y_2 - y_1)/2h = 0.2$, $\nu = 0.30$.

	Case 1		Case 2		Case 3		Case 4
y_1/d	$K_{In(k)}$	$\varepsilon_I^{(1)}$	$K_{In(k)}$	$\varepsilon_I^{(2)}$	$K_{In(k)}$	$\varepsilon_I^{(3)}$	$K_{In(k)}$
0.1	$-0.07804_{(6)}$	0.8461	$-0.07848_{(5)}$	0.2857	$-0.07862_{(6)}$	0.1030	$-0.07870_{(5)}$
0.2	$-0.07266_{(5)}$	1.0187	$-0.07280_{(4)}$	0.8223	$-0.07328_{(4)}$	0.1639	$-0.07340_{(5)}$
0.4	$-0.06053_{(4)}$	0.8740	$-0.06071_{(4)}$	0.5716	$-0.06103_{(4)}$	0.0487	$-0.06106_{(4)}$
0.6	$-0.04546_{(4)}$	0.7932	$-0.04558_{(4)}$	0.5323	$-0.04583_{(4)}$	0.0067	$-0.04583_{(4)}$
0.8	$-0.02957_{(4)}$	0.7928	$-0.02967_{(4)}$	0.4499	$-0.02979_{(4)}$	0.0424	$-0.02980_{(4)}$
1.0	$-0.01483_{(4)}$	0.7275	$-0.01491_{(4)}$	0.1854	$-0.01498_{(4)}$	0.3258	$-0.01494_{(4)}$
1.2	$-0.00215_{(4)}$	5.1374	$-0.00222_{(5)}$	2.0837	$-0.00225_{(4)}$	0.6077	$-0.00227_{(4)}$
1.4	$0.00828_{(4)}$	0.6468	$0.00823_{(4)}$	1.2643	$0.00830_{(4)}$	0.4527	$0.00834_{(4)}$
1.6	$0.01668_{(4)}$	0.3797	$0.01665_{(4)}$	0.5563	$0.01676_{(4)}$	0.1247	$0.01674_{(4)}$

TABLE 3 Normalized mode-(2) SIF results and relative errors $V_0 = 0.05$, $d/h = 0.8$, $\eta = 0.3$, $\beta_1 = -0.0569$, $\beta_2 = 0.218$, $\beta_3 = 0.0371$, $(y_2 - y_1)/2h = 0.2$, $\nu = 0.30$.

	Case 1		Case 2		Case 3		Case 4
y_1/d	$K_{IIn(k)}$	$\varepsilon_{II}^{(1)}$	$K_{IIn(k)}$	$\varepsilon_{II}^{(2)}$	$K_{IIn(k)}$	$\varepsilon_{II}^{(3)}$	$K_{IIn(k)}$
0.1	$0.15367_{(6)}$	0.1855	$0.15424_{(5)}$	0.1808	$0.15399_{(6)}$	0.0208	$0.15396_{(5)}$
0.2	$0.14043_{(5)}$	0.5029	$0.14059_{(4)}$	0.3890	$0.14081_{(4)}$	0.2299	$0.14114_{(5)}$
0.4	$0.11026_{(4)}$	0.2792	$0.11058_{(4)}$	0.0094	$0.11064_{(4)}$	0.0624	$0.11057_{(4)}$
0.6	$0.08181_{(4)}$	0.0158	$0.08177_{(4)}$	0.0649	$0.08186_{(4)}$	0.0429	$0.08183_{(4)}$
0.8	$0.05834_{(4)}$	0.2164	$0.05838_{(4)}$	0.1481	$0.05848_{(4)}$	0.0224	$0.05847_{(4)}$
1.0	$0.04083_{(4)}$	0.3295	$0.04086_{(4)}$	0.2615	$0.04096_{(4)}$	0.0120	$0.04097_{(4)}$
1.2	$0.02822_{(4)}$	0.4922	$0.02825_{(5)}$	0.3645	$0.02835_{(4)}$	0.0707	$0.02836_{(4)}$
1.4	$0.01925_{(4)}$	0.7448	$0.01929_{(4)}$	0.5575	$0.01939_{(4)}$	0.0461	$0.01940_{(4)}$
1.6	$0.01290_{(4)}$	1.1585	$0.01294_{(4)}$	0.8551	$0.01305_{(4)}$	0.0612	$0.01306_{(4)}$

defined relative to the numerical results of this case in the following form:

$$\varepsilon_I^{(j)} = \left| \frac{K_{In(k)}^{(j)} - K_{In(k)}^{(4)}}{K_{In(k)}^{(4)}} \right| \times 100, \tag{41}$$

$$\varepsilon_{II}^{(j)} = \left| \frac{K_{IIn(k)}^{(j)} - K_{IIn(k)}^{(4)}}{K_{IIn(k)}^{(4)}} \right| \times 100, \quad j = 1, 2, 3,$$

where the superscript (j) stands for the case number, and the subscript (k) shows the number of iterations required in the main algorithm given in Figure 4 to compute convergent SIFs. Note that all approximate percent errors computed for Case 3 are smaller than 1%. Computation time required for a Case 4 mesh is in general two times that needed for Case 3. Thus, considering degree of accuracy, convergence, and computational cost, Case 3 is assessed to

be the optimum choice for computational analyses. The results provided in Sections 4.2 and 4.3 are thus generated by using the Case 3 mesh configuration for which the total number of elements is 122,086. In all cases, the number of singular elements utilized for the first row circle around the crack tip is 24 and those for the second row circle around the crack tip is 48, which results in 72 elements in total.

4.2 | Verification

The numerical results generated in the present study are verified by comparisons to the results available in the literature. Figure 6 depicts mode-(1) and mode-(2) SIFs obtained by present study and those available in the open literature for various values of y_1/d. In these comparisons, there is no frictional heat generation; hence, problem is treated under isothermal conditions.
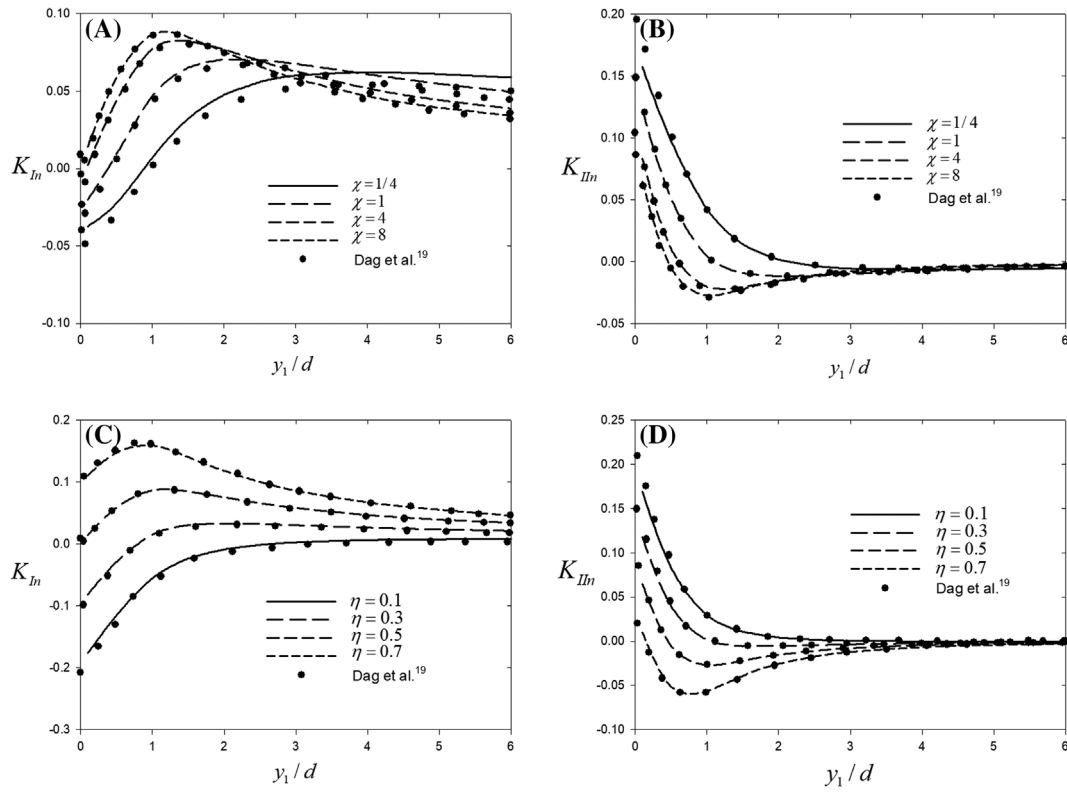
FIGURE 6 (A,B) Normalized SIFs versus y_1/d for different χ, $\eta = 0.5$. (C,D) Normalized SIFs versus y_1/d for different η, $\chi = 8$; $(y_2 - y_1)/d = 1.0$, $d/h = 1.0$, $\kappa_1 = \kappa_2 = 2.0$.

Figure 6A,B illustrates the normalized mode-(1)and mode-(2) SIFs with respect to y_1/d for different values of materials' shear modulus ratio. In these comparisons depicted in Figure 6, material model for the FGM coating has an exponential variation of the form $\mu_1(x) = \mu_1^0 \exp(\beta_1 x)$, which was provided in Equation (32), and χ indicates the shear modulus ratio of materials utilized in the FGM, which reads

$$\chi = \frac{\mu_1^h}{\mu_1^0} = \exp(\beta_1 h). \qquad (42)$$

Figure 6C,D shows the normalized mode-(1) and mode-(2) SIFs with respect to y_1/d as functions of friction coefficient η considering an exponential-type FGM coating. Poisson's ratio of the material is assumed to be constant $\nu = 0.25$, which leads to $\kappa = 2.0$ in plane strain condition. As can be inferred from following figure (see Figure 6), SIFs obtained in the present study display a very good agreement with those obtained by Dag et al.[19]

4.3 | Parametric studies

In this section, results of parametric studies are presented. Influences of punch speed, material property variations

(metal rich [MR], linear [L], and ceramic rich [CR]), coefficient of friction, punch width, and crack length on normalized SIFs are investigated in detail. Spatial variations of the thermomechanical properties of the graded coating are expressed by a power law function as follows (Dag[30]):

$$\mu_1(x) = \mu_1^0 + \left(\mu_1^h - \mu_1^0\right)\left(\frac{x}{h}\right)^{\gamma_1}, \ 0 \le x \le h, \qquad (43)$$

$$k_1(x) = k_1^0 + \left(k_1^h - k_1^0\right)\left(\frac{x}{h}\right)^{\gamma_2}, \ 0 \le x \le h, \qquad (44)$$

$$\alpha_1(x) = \alpha_1^0 + \left(\alpha_1^h - \alpha_1^0\right)\left(\frac{x}{h}\right)^{\gamma_3}, \ 0 \le x \le h, \qquad (45)$$

$$\mu_2(x) = \mu_1^h, \ h \le x \le \infty, \qquad (46)$$

$$k_2(x) = k_1^h, \ h \le x \le \infty, \qquad (47)$$

$$\alpha_2(x) = \alpha_1^h, \ h \le x \le \infty, \qquad (48)$$

where material parameters with the subscript ()$_1$ given by Equations (43)–(48), respectively, denote the shear modulus, thermal conductivity, and coefficient of thermal expansion for the coating and those with subscript ()$_2$ indicate same material parameters for the homogeneous

half-plane. Parameters with superscript $()^0$ indicate the properties of graded coating on the contact surface in which $x = 0$, and parameters given by superscript $()^h$ denote the properties of the coating at the interface. The inhomogeneity variation profiles of the graded coating is governed by exponents γ_i, $(i = 1, 2, 3)$. In parametric studies shown in the following subsections, power-law FGM model was utilized for the coating material in which variation through the thickness of the coating is illustrated in Figure 7. In this configuration, the upper and lower surfaces consist of 100% ceramics and 100% metal, respectively. ZrO_2 and Ti-6Al-4V given in Table 1 are utilized as ceramic and metal. γ_1 shows the gradient index, and $\mu_1(x)/\mu_1^0$ indicates the ratio of coating shear modulus to surface material shear modulus consisting of 100% ceramic. $\gamma_1 < 1.0$ shows MR, $\gamma_1 > 1.0$ displays CR, and $\gamma_1 = 1.0$ indicates the linear distribution.

Figure 8 demonstrates deformed mesh around the contact region when crack length is adjusted to $d/h = 0.8$.

As friction coefficient is increased from $\eta = 0.1$ to $\eta = 0.7$, the lateral force acting the rigid punch is increased and hence results in a much crack opening displacement at the crack mouth. Deformed mesh configuration for an MR graded coating is obtained in Figure 8A–D, and that for a CR coating is presented in Figure 8E–H. As observed from the figures, the deformation due to the indentation of the frictional punch is greater for an MR coating when compared to CR one, as excpected. Since ceramics has a larger elastic modulus, deformation and the crack opening displacement become smaller.
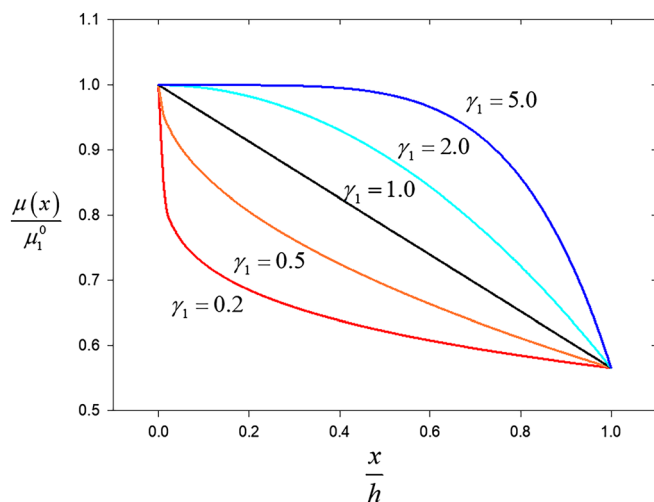

FIGURE 7 Representation of the ceramic-rich (CR), linear (L), and metal-rich (MR) variations of the properties in the graded coating. [Colour figure can be viewed at wileyonlinelibrary.com]

4.3.1 | Effect of punch sliding speed

In this section, temperature contours and nondimensional SIFs are presented for different punch sliding speeds. Figure 9A–D shows temperature contours around the contact and crack regions on deformed mesh for an MR coating. y_1/d is taken small since the critical condition is the case where the trailing edge of the punch is closer to surface crack. When punch speed is increased, temperature around the contact region is increased. In stationary case where $V_0 = 0.0$, there is no heat generation due to the sliding of punch. Hence, the indentation depth and crack opening displacement are observed maximum as described in Figure 9A. However, for the case where punch speed is $V_0 = 0.20$, temperature values around the contact region increases due to the larger amount of frictional heat, and this heat leads to much thermal expansion around contact and crack regions. Temperature values around the trailing end of the contact are greater. In this case, indentation depth and crack opening displacement tend to become smaller due to thermal deformation as depicted in Figure 9D.

Figure 9E–H indicates the temperature contours around the contact region in the case of a CR coating. When punch sliding speed is increased, temperature within the contact region is increased again. When temperature contours in Figure 9E–H are compared with those obtained in Figure 9A–D, it can be said that much heat has dissipated through the coating material in MR case rather than CR case due to the larger thermal conductivity of the metal. Hence, the level of temperature at the contact surface is greater, and temperature through the depth is lower for the CR case, which implies a kind of thermal barrier coating.

For the graded coating with MR shear modulus variation $\gamma_1 = 1/5$, punch sliding speed affect the mode-(1) and mode-(2) SIFs. As punch sliding speed is increased, normalized mode-(1) SIF is increased for all values of y_1/d as observed in Figure 10A. Mode-(1) SIF takes its highest values around $y_1/d = 3.0 - 4.0$. When mode-(2) SIF is examined in Figure 10B, it seems that punch sliding speed does not considerably affect the mode-(2) SIF values. Increase in the punch speed results in a small increase in mode-(2) SIF when punch is close to the surface crack especially in $y_1/d = 0.0 - 2.0$.

For the graded coatings with linear shear modulus variation $\gamma_1 = 1$, the influence of punch speed on mode-(1) SIF depicted in Figure 10C is greater when compared to the case in which $\gamma_1 = 1/5$ in Figure 10A since larger level of mode-(1) SIF values are obtained at the same punch speed. The impact of punch speed on mode-(2) SIF for the linear variation of shear modulus is also slightly greater.

(A) **(B)** **(C)** **(D)** **(E)** **(F)** **(G)** **(H)**
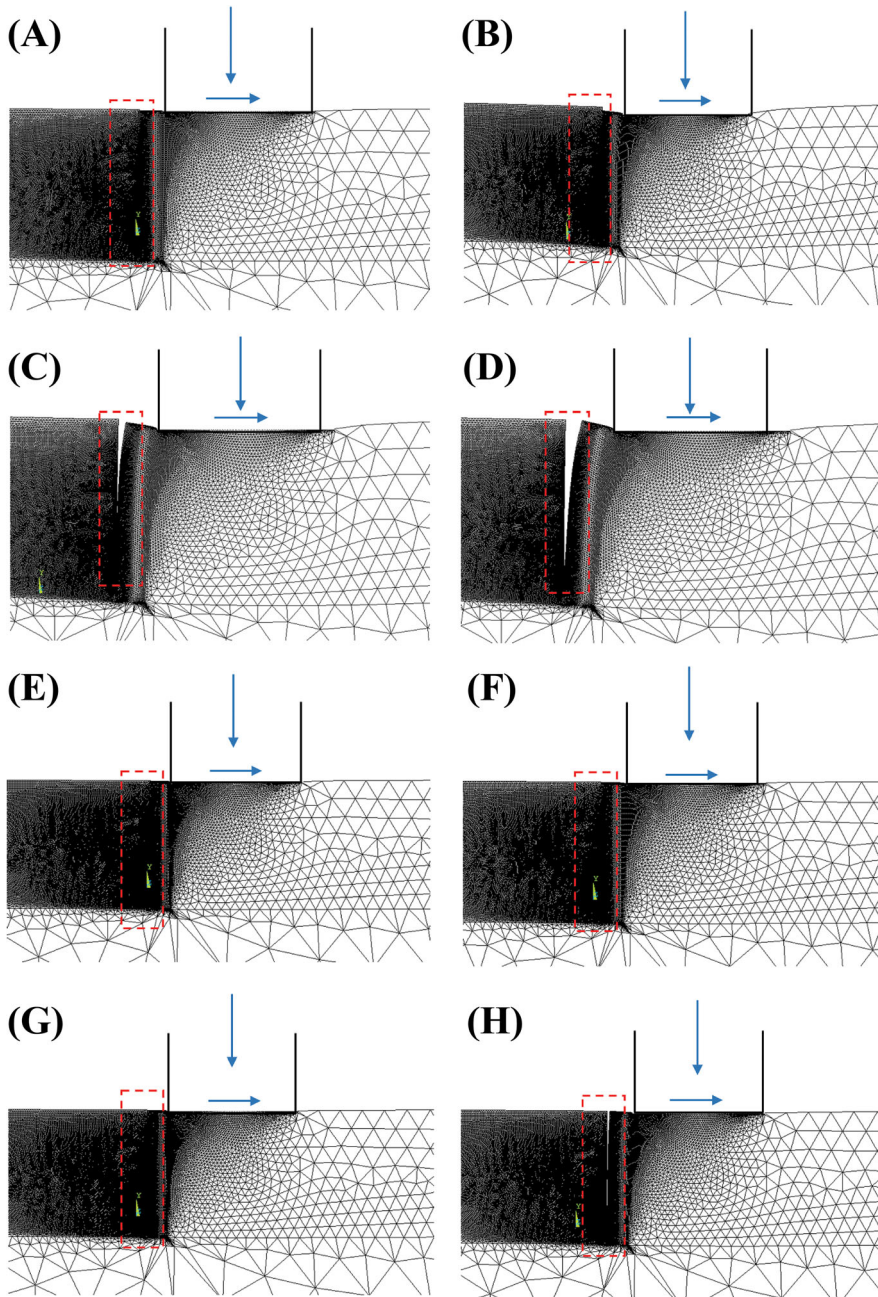
FIGURE 8 Deformed mesh around the surface crack and the contact zones for (A–D) metal-rich FGM coating, $\gamma_1 = \gamma_2 = \gamma_3 = 1/5$, (A) $\eta = 0.1$, (B) $\eta = 0.3$, (C) $\eta = 0.5$, (D) $\eta = 0.7$; (E–H) ceramic-rich FGM coating, $\gamma_1 = \gamma_2 = \gamma_3 = 5$, (E) $\eta = 0.1$, (F) $\eta = 0.3$, (G) $\eta = 0.5$, (H) $\eta = 0.7$; $V_0 = 0.10$, $(y_2 - y_1)/2h = 0.5$, $d/h = 0.8$, $y_1/d = 0.2$, $\kappa_1 = \kappa_2 = 1.8$. [Colour figure can be viewed at wileyonlinelibrary.com]

Figure 10E–F indicates mode-(1) and mode-(2) SIFs for the graded coating with ceramic rich shear modulus distribution. Obtained mode-(1) SIF values for $\gamma_1 = 5.0$ are greater than those calculated for other cases $\gamma_1 = 1/5$ and $\gamma_1 = 1$. The maximum value of the mode-1 SIF is observed around $y_1/d = 3.0$ in all cases. It is seen that the amount of increase in mode-(1) SIF due to the punch speed is greater at $\gamma_1 = 5$ when compared to that observed for other cases, that is, $\gamma_1 = 1/5$ and $\gamma_1 = 1$. The influence of punch speed on mode-(2) SIF is seen minimal as shown in Figure 10F, but mode-(2) SIF slightly increases in the interval between $y_1/d = 0.0$ and $y_1/d = 2.0$. It is

obvious that higher punch speed results in a greater change in the mode-(2) SIF.

4.3.2 | Effect of coefficient of friction

In this part, effect of coefficient of friction on normalized mode-(1) and mode-(2) SIFs is examined. Figure 11 demonstrates this effect on normalized SIFs for coatings with an MR and a CR shear modulus, respectively. It can be inferred from Figure 11A,B that friction coefficient plays a very important role on both mode-(1) and mode-

FIGURE 9 Temperature contours around the surface crack and the contact zones $(y_2 - y_1)/2h = 0.5$, $d/h = 0.8$, $y_1/d = 0.2$, $\eta = 0.5$, $\kappa_1 = \kappa_2 = 1.8$, (A–D) $\gamma_1 = 1/5$, $\gamma_2 = 1/5$, $\gamma_3 = 1/5$; (E–H) $\gamma_1 = 5$, $\gamma_2 = 5$, $\gamma_3 = 5$; (A,E) $V_0 = 0.0$, (D,F) $V_0 = 0.05$, (C,G) $V_0 = 0.10$, (D,H) $V_0 = 0.20$. [Colour figure can be viewed at wileyonlinelibrary.com]
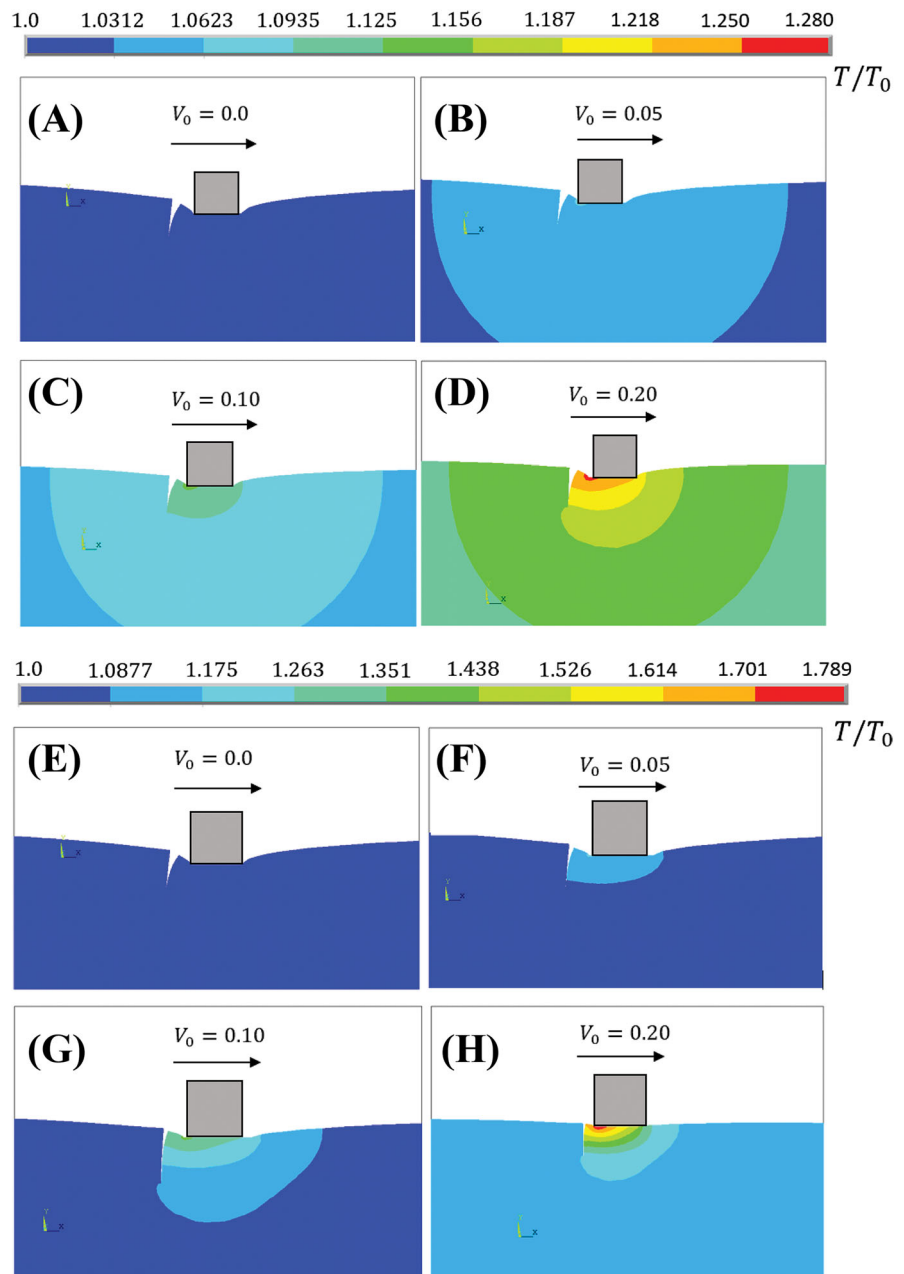
(2) SIFs. It is significant to say that for friction coefficient values $\eta = 0.1 - 0.3$, mode-I SIF values are negative when punch is close to the crack, which implies that there is a crack closure in that region. As η is increased, the mode-(1) SIF is escalated for all values of y_1/d. Use of larger coefficient of friction induces a greatest increase in mode-(1) SIF around $y_1/d = 1.5$. Hence, this location is critical, and surface coating is vulnerable to possible failures when punch stands at this site. As y_1/d is increased, mode-(1) SIF smoothly decreases since punch moves away from the crack mouth. Figure 11B shows the mode-(2) SIF as functions of surface friction coefficient η. When

η is increased, the level of mode-(2) SIF is decreased, and the maximum decrease in mode-(2) SIF is seen around $y_1/d = 1.5$. Moreover, increase in the coefficient of friction leads to negative values of mode-(2) SIF especially for $\eta = 0.7$ Figure 11C,D displays the mode-(1) and mode-(2) SIFs for different values of η. When $\gamma_1 = 5$, increase in the surface friction results in a greater change in mode-(1) SIF since K_{In} reaches 0.19 at $\eta = 0.7$, but this value is around 0.14 for $\gamma_1 = 1/5$. Mode-(2) SIF is presented in Figure 11D that increase in η results in a decrease in K_{IIn}, but this decrease is less when compared to that seen in Figure 11B.
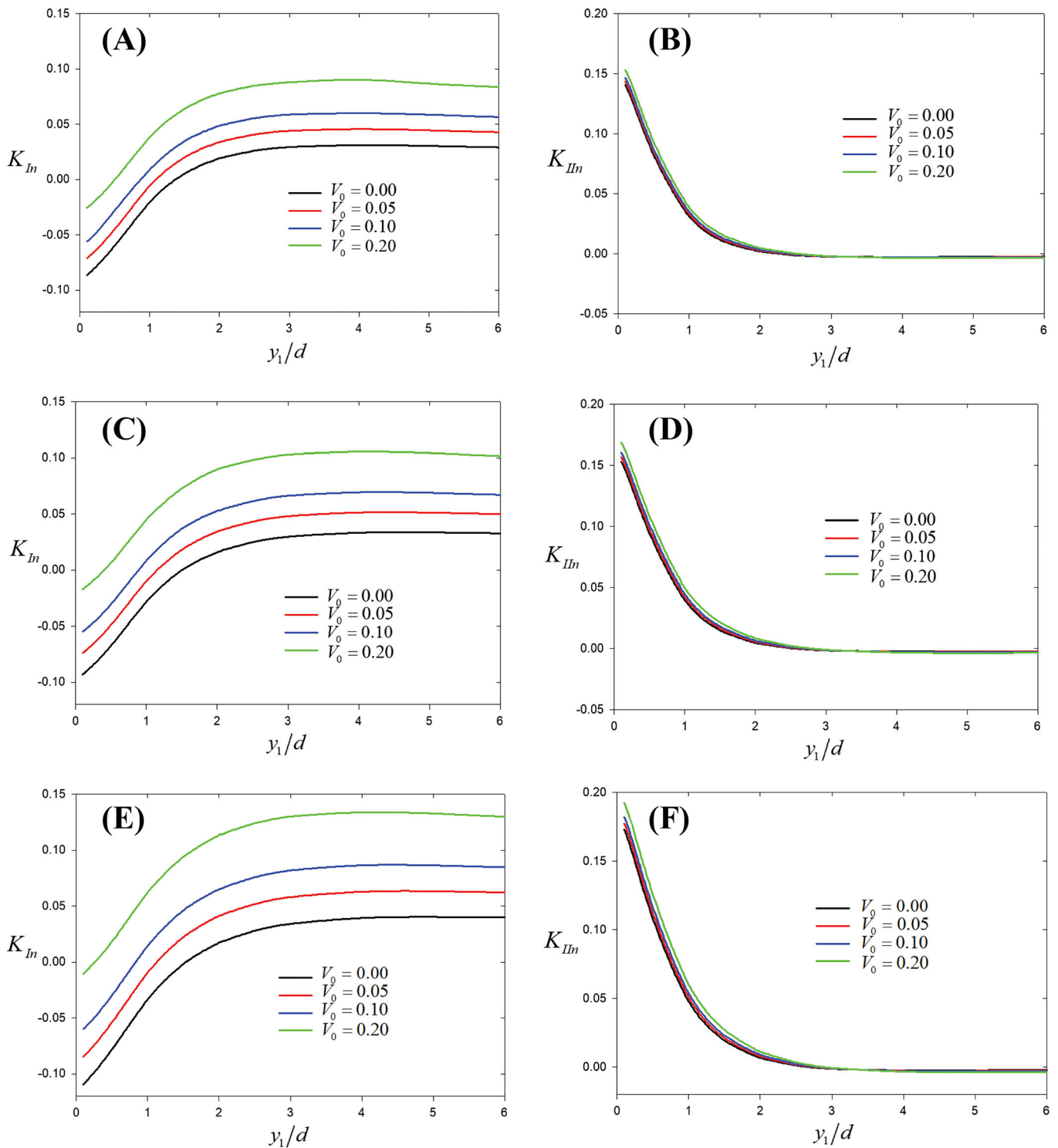
FIGURE 10 Effect of punch sliding speed on normalized mode-(1) and mode-(2) SIFs (A,B) $\gamma_1 = 1/5$, (C,D) $\gamma_1 = 1$, (E,F) $\gamma_1 = 5$, $\gamma_2 = \gamma_3 = 2.0$, $(y_2 - y_1)/2h = 0.5$, $d/h = 0.8$, $\eta = 0.3$, $\kappa_1 = \kappa_2 = 1.8$. [Colour figure can be viewed at wileyonlinelibrary.com]

4.3.3 | Effect of power-law exponents for material's thermoelastic properties

The effect of material shear modulus variation on normalized mode-(1) and mode-(2) SIFs is examined. γ_1 controls the variation of shear modulus in the coating. As γ_1 is increased, the mode-(1) SIF is increased at all points of punch locations. For all cases of γ_1, mode-I SIF is negative in the region $y_1/d = 0.0 - 0.5$, which implies crack closure. The impact of γ_1 on mode-(1) SIF K_{In} tends to be
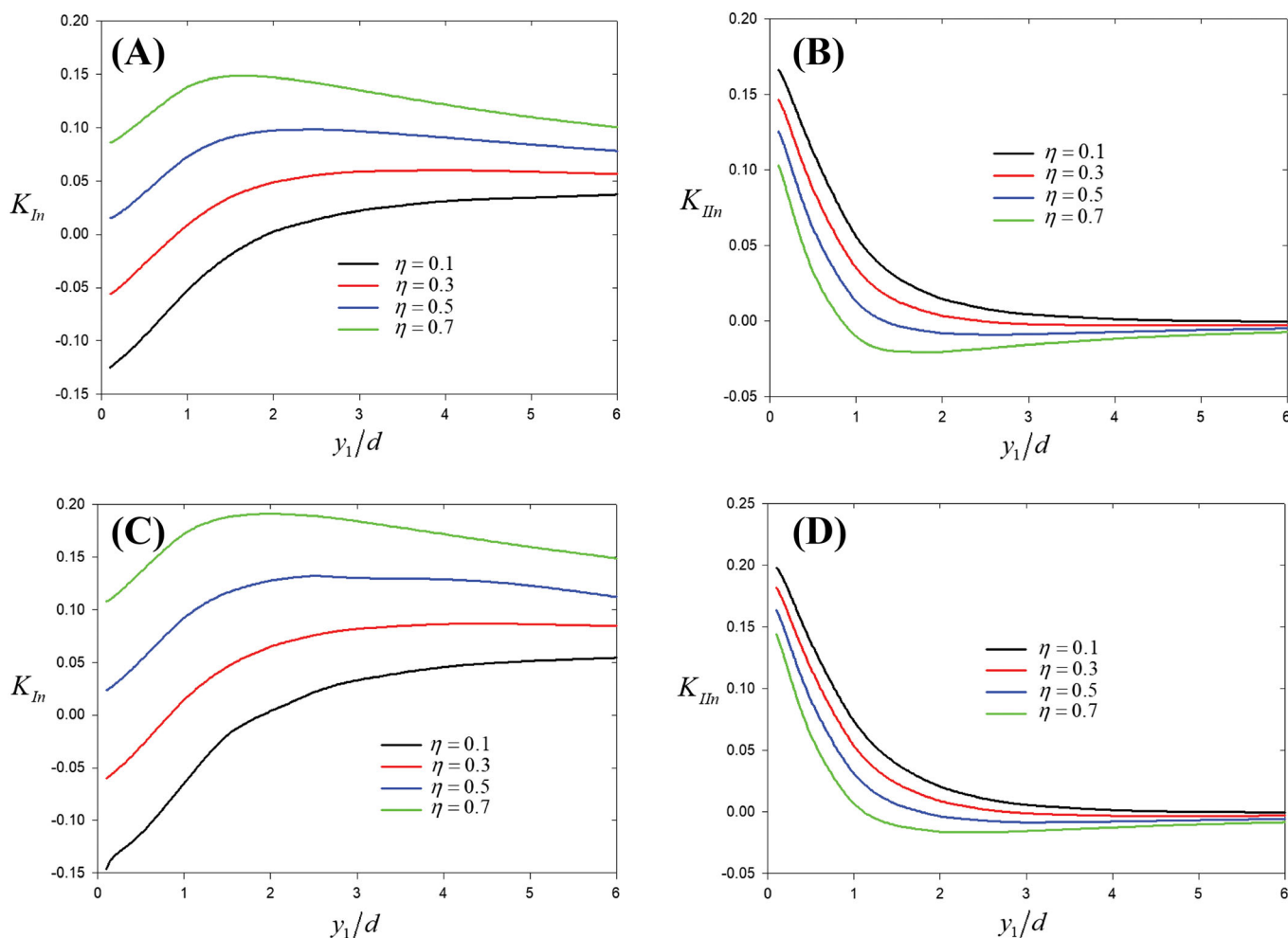
FIGURE 11 Effect of coefficient of friction η on normalized mode-(1) and mode-(2) SIFs, (A,B) $\gamma_1 = 1/5$, (C,D) $\gamma_1 = 5$; $\gamma_2 = \gamma_3 = 2.0$, $(y_2 - y_1)/2h = 0.5$, $d/h = 0.8$, $V_0 = 0.10$, $\kappa_1 = \kappa_2 = 1.8$. [Colour figure can be viewed at wileyonlinelibrary.com]

remarkable when punch stands at points greater than $y_1/d = 2.0$. It can be observed in Figure 12A,B that mode-(1) SIF reaches high levels for the coating with CR shear modulus $\gamma_1 = 5.0$. It is worthy to say that coating with CR shear modulus case are seems susceptible to possible surface cracking failure due to the higher values of mode-(1) SIF. Relatively higher values of mode-(1) SIF occurs in the interval from $y_1/d = 2.0$ to $y_1/d = 6.0$. Thus, the location of the punch in this interval is critical. Mode-(2) SIF is shown in Figure 12B, and K_{IIn} is increased at all points as γ_1 is increased. Moreover, K_{IIn} can be reduced to negative levels at $y_1/d > 3.0$. Difference between SIFs calculated for different γ_1 values gradually diminishes as y_1/d gets larger values.

The influence of thermal conductivity variation on SIFs is analyzed. γ_2 controls the thermal conductivity profile within the coating. Mode-(1) and mode-(2) SIFs are obtained as functions of γ_2, and they are depicted in Figure 12C,D. Increase in the ratio γ_2 leads to a decrease in K_{In}, while it results in very slight increase in K_{IIn}.

Change in the mode-(1) SIF due to γ_2 is greater than that observed in the mode-(2) SIF. Hence, it can be said that mode-(1) SIF (K_{In}) is more sensitive to the change in the materials' thermal conductivity variation within the coating. Utilization of a coating with CR thermal conductivity, that is, lower values of thermal conductivity, leads to decrease in mode-(1) SIF, so this will help to improve the contact damage originating from crack propagation. It can be inferred from Figure 12D that as γ_2 is increased, mode-(2) SIF slightly increases for all values of y_1/d.

Figure 12E,F describes the normalized mode-(1) and mode-(2) SIFs as functions of γ_3. The parameter γ_3 controls the thermal expansion coefficient variation in the coating. The change in mode-(1) SIF due to the variation of γ_3 is greater than that observed in the mode-(2) SIF. Hence, changing the thermal expansion profile from the MR case to the CR case has a greater influence on mode-(1) SIF. Although increase in γ_3 induces notable increase in mode-(1) SIF, it results in a very slight decrease in mode-(2) SIF.
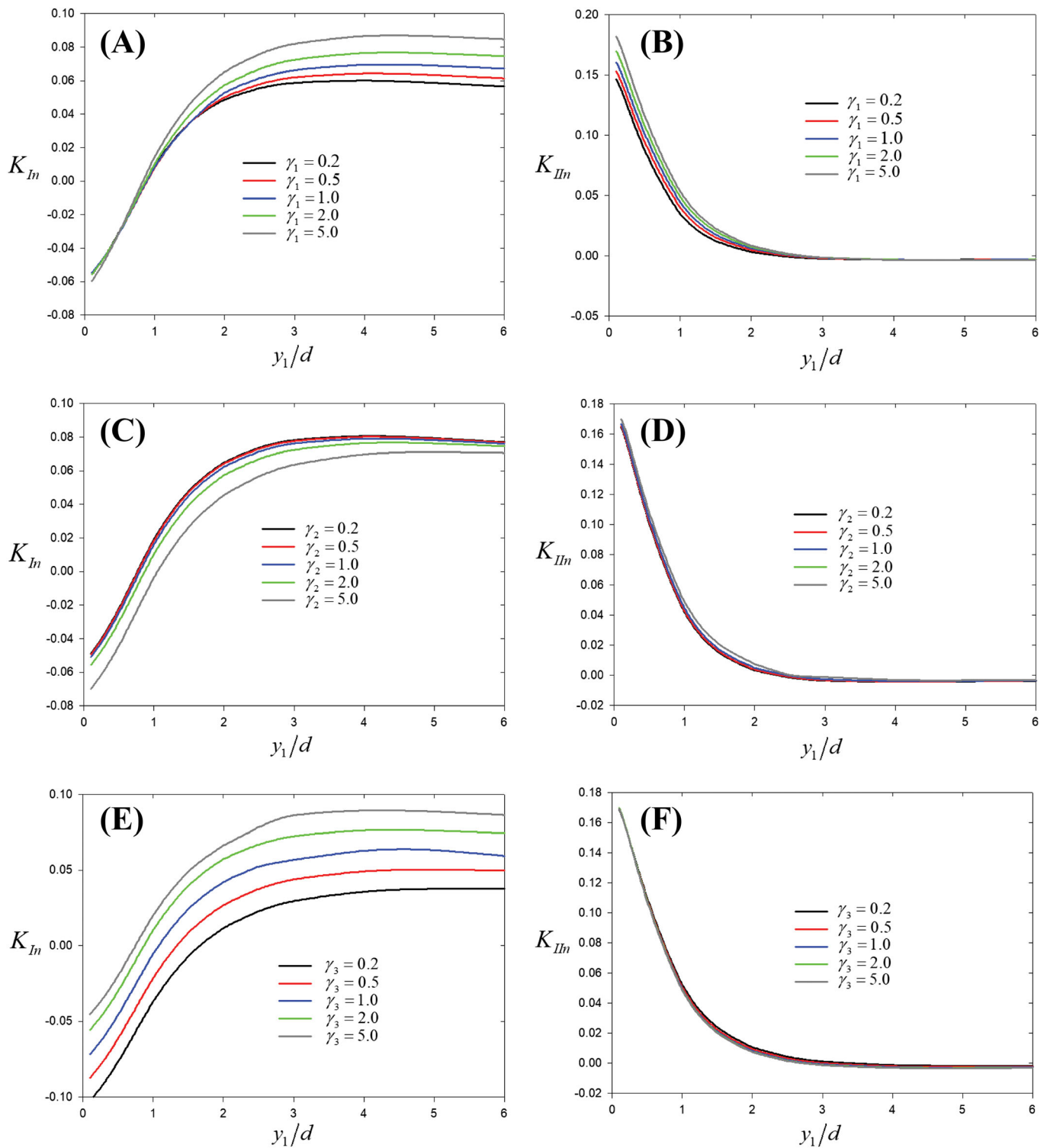
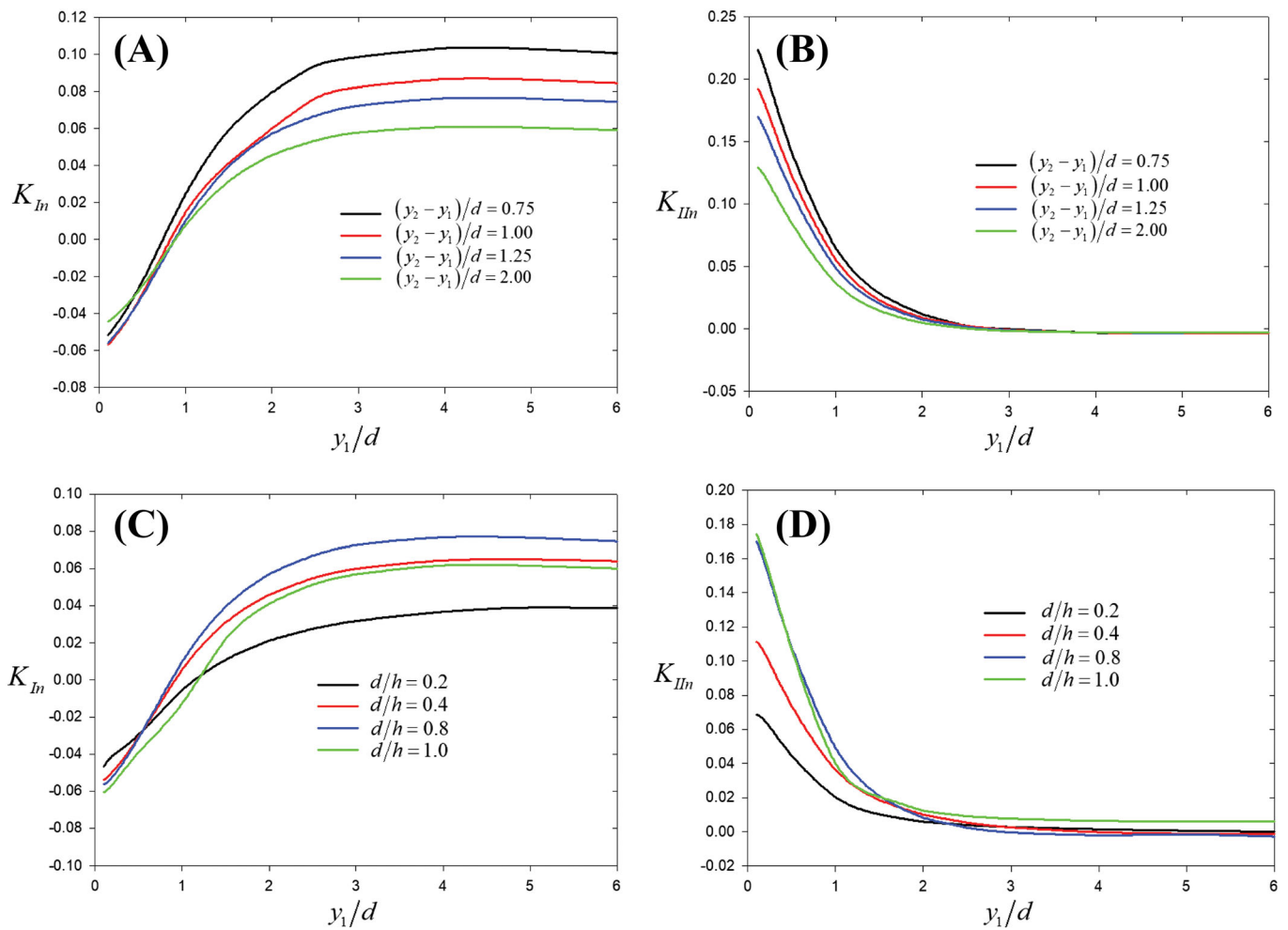**FIGURE 12** (A,B) Effect of γ_1 on normalized mode-(1) and mode-(2) SIFs $\gamma_2 = \gamma_3 = 2.0$. (C,D) Effect of γ_2 on normalized mode-(1) and mode-(2) SIFs $\gamma_1 = \gamma_3 = 2.0$. (E,F) Effect of γ_3 on normalized mode-(1) and mode-(2) SIFs $\gamma_1 = \gamma_2 = 2.0$; $V_0 = 0.10$, $(y_2 - y_1)/2h = 0.5$, $d/h = 0.8$, $\eta = 0.3$, $\kappa_1 = \kappa_2 = 1.8$. [Colour figure can be viewed at wileyonlinelibrary.com]

FIGURE 13 (A,B) Effect of punch width on normalized mode-(1) and mode-(2) SIFs $d/h = 0.8$. (C,D) Effect of crack length on dimensionless mode-(1) and mode-(2) SIFs $(y_2 - y_1)/2h = 0.5$; $V_0 = 0.10$, $\gamma_1 = \gamma_2 = \gamma_3 = 2.0$, $\eta = 0.3$, $\kappa_1 = \kappa_2 = 1.8$. [Colour figure can be viewed at wileyonlinelibrary.com]

It can be said that utilization of coating possessing a CR thermal expansion coefficient profile results in greater mode-(1) SIF, which implies that coatings with relatively lower thermal expansion coefficient will be susceptible to failures arising from surface crack. Hence, in order to reduce K_{In}, thermal expansion coefficient within the coating should be increased.

4.3.4 | Effect of punch and surface crack dimensions

The effect of punch width on normalized mode-(1) and mode-(2) SIFs is investigated in this section. As can be inferred from the Figure 13A,B that change in the punch width significantly influences the mode-(1) and mode-(2) SIFs. For relatively narrow

punches (i.e., $(y_2 - y_1)/d = 0.75$), the mode-(1) and mode-(2) SIFs take their highest values at all points of y_1/d. As punch width is increased from $(y_2 - y_1)/d = 0.75$ to $(y_2 - y_1)/d = 2.0$, mode-(1) and mode-(2) SIFs decrease for all values of y_1/d. This conclusion is expected since relatively wider punch results in a lower amount of contact stresses and consequently lower heat generation on the contact surface. Major change in mode-(2) SIF is observed in the region $y_1/d = 0$ to $y_1/d = 2$, which infers that critical sites due to mode-(2) cracking are points close to the crack mouth. The effect of surface crack length on normalized mode-(1) and mode-(2) SIFs is investigated in Figure 13C,D. The ratio d/h is introduced, which implies the ratio between crack length and coating thickness. Results for mode-(1) and mode-(2) SIFs are shown as functions of d/h with respect to various y_1/d. When $d/h = 1.0$, the surface crack lies along the

thickness of the coating, and its tip touches at the interface. If $d/h = 0.2 - 0.8$, the tip of the surface crack is embedded in the coating.

As the ratio d/h is increased, K_{In} is decreased and falls below zero at closer points to the contact $y_1/d = 0 - 0.5$. However, increase in d/h results in an increase, and further increase of this ratio to $d/h = 1.0$ induces remarkable decrease for $y_1/d > 0.5$. The same trend is observed in the mode-(2) SIF, which implies that increase in d/h leads to increase and further increase in this ratio causes a sharp decrease, again.

5 | CONCLUSION

In the present study, the surface crack existing on FGM coating/homogeneous substrate system subjected to the frictional contact with heat generation was analyzed computationally based on FEM. Contact and a surface crack problem are modeled using finite elements. Quadrilateral elements are utilized for the elastic medium, contact and target elements are used to discretize the contact surface, and singular elements are employed for the crack problem. Contact problem is solved iteratively until frictional heat on the contact surface reaches steady state. When the difference between heat flux calculated at present iteration and that calculated at previous iteration becomes an acceptable level, iterative program stops. In addition to contact problem, a crack is included on the surface of the FGM coating. Mode-(1) and mode-(2) SIFs at the tip of a surface crack are computed utilizing the DCT. Present study put forward a novel computational method which is able to perform calculations for mode-(1) and mode-(2) SIFs for various thermoelastic contact loading conditions. Comparisons with other studies in the open literature show a very good agreement between results. Hence, verification of the developed method is satisfied. Then, case studies are carried out to understand the main impacts of various parameters such as punch speed, coefficient of friction, punch width, material's thermoelastic properties, and punch/crack dimensions on normalized SIFs. The following conclusions can be drawn from this study:

- Increase in the punch speed induces increase in the frictional heat on the contact region. In isothermal case where $V_0 = 0.0$, deformation of the contact surface and crack opening displacement is greater than those observed in sliding condition $V_0 > 0$ since generated heat on the surface causes thermal expansion in the coating material. As the speed of punch is increased, normalized mode-(1) SIF values increase for all MR, linear and CR shear modulus cases. The greatest change in mode-(1) SIF is observed coatings with CR shear modulus case $\gamma_1 = 5.0$. Increase in punch speed results in a slight change in mode-(2) SIF when compared to mode-(1) SIF.

- Utilization of coatings with metal rich shear modulus $\gamma_1 = 1/5$ can be sensible selection to avoid possible surface cracking failure since obtained mode-(1) SIF values are less than those calculated for other types $\gamma_1 = 1$ and $\gamma_1 = 5$. Moreover, coatings with MR shear modulus distribution exhibits relatively less sensitive SIF variation with respect to punch speed. Hence, coating with an MR shear modulus variation can be said to be more durable in thermoelastic contacts.

- As coefficient of friction is increased, normalized mode-(1) SIF is increased, while normalized mode-(2) SIF is decreased.

- When punch width is increased, it induces less stress on the contact surface. As a result, less heat generation occurs on the contact surface. Mode-(1) and mode-(2) SIFs tend to decrease.

- As the power law exponent for the shear modulus γ_1 is increased, both mode-(1) and mode-(2) SIFs are increased.

- Increase in the power law exponent for the thermal conductivity γ_2 leads to a considerable decrease in the mode-(1) SIF, while it leads to very slight increase in mode-(2) SIF.

- The impact of the power law exponent for thermal expansion coefficient γ_3 on SIFs is notable. As γ_3 is increased, the mode-(1) SIF is considerably increased whereas the mode-(2) SIF is slightly decreased.

- The length of the surface crack has a profound effect on SIFs. As d/h is increased, mode-(1) and mode-(2) SIFs are increased. However, further increase in the crack length–coating thickness ratio d/h to 1.0 results in a significant decrease in these two factors.

The method developed in this study will be helpful in understanding the fracture characteristics of FGM coatings under the effect of thermoelastic sliding conditions. Examination of the influence of frictional heat generation on SIFs of a surface crack tip is new in the literature. Hence, results of present study are believed to be useful in analysis and design of FGM coatings in tribological applications.

CONFLICT OF INTEREST STATEMENT

The authors declare that they have no known competing financial interests or personal relationships that could have appeared to influence the work reported in this paper.

ORCID

Mehmet N. Balci ⓘ https://orcid.org/0000-0002-4416-6761

REFERENCES

1. Johnson KL. *Contact Mechanics*. Cambridge University Press; 1985.
2. Hills DA, Nowel D, Sackfield A. *Mechanics of Elastic Contacts*. Butterworth- Heinemann; 1993.
3. Hills DA, Sackfield A. Sliding contact between dissimilar elastic cylinders. *J Tribol*. 1985;107(4):463-466.
4. Giannakopulos AE, Suresh S. Indentation of solids with gradients in elastic properties: part I. point force. *Int J Solids Struct*. 1997;34(19):2357-2392.
5. Giannakopulos AE, Suresh S. Indentation of solids with gradients in elastic properties: part II. Axisymmetric indenters. *Int J Solids Struct*. 1997;34(19):2393-2428.
6. Suresh S, Giannakopoulos AE, Alcala J. Spherical indentation of compositionally graded materials: theory and experiments. *Acta Mater*. 1997;45(4):1307-1321.
7. Giannakopulos AE, Pallot P. Two dimensional contact analysis of elastic graded materials. *J Mech Phys Solids*. 2000; 48(8):1597-1631.
8. Guler MA, Erdogan F. Contact mechanics of graded coatings. *Int J Solids Struct*. 2004;41(14):3865-3889.
9. Guler MA, Erdogan F. The frictional sliding contact problem of rigid parabolic and cylindrical stamps on graded coatings. *Int J Mech Sci*. 2007;49(2):161-182.
10. Guler MA, Erdogan F. Contact mechanics of two deformable elastic solids with graded coatings. *Mech Mater*. 2006;38: 663-647.
11. Apatay T, Dag S, Guler MA, Gulgeç M. Subsurface contact stresses in functionally graded coatings loaded by a frictional flat stamp. *J Fact Eng Arch Gazi Univ*. 2010;25(3):611-623.
12. Dag S, Guler MA, Yildirim B, Cihan Ozatag A. Sliding frictional contact between a rigid punch and a laterally graded elastic medium. *Int J Solids Struct*. 2009;46(22-23):4038-4053.
13. Ke L-L, Wang Y-S. Two-dimensional contact mechanics of functionally graded materials with arbitrary spatial variations of material properties. *Int J Solids Struct*. 2006;43(18-19):5779-5798.
14. Ke L-L, Wang Y-S. Two-dimensional sliding frictional contact of functionally graded materials. *Eur J Mech a/Solids*. 2007; 26(1):171-188.
15. Dag S. Consideration of spatial variation of the friction coefficient in contact mechanics analysis of laterally graded materials. *Z Angew Math Mech*. 2016;96(1):121-136.
16. El-Borgi S, Abdelmoula R, Keer L. A receding contact plane problem between a functionally graded layer and a homogenous substrate. *Int J Solids Struct*. 2006;43(3-4):658-674.
17. El-Borgi S, Usman S, Guler MA. A frictional receding contact plane problem between a functionally graded layer and a homogenous substrate. *Int J Solids Struct*. 2014;51(25-26):4462-4476.
18. Choi HJ, Paulino GH. Interfacial cracking in a graded coating/substrate system loaded by a frictional sliding flat punch. *Proc R Soc a*. 2010;466(2115):853-880.
19. Dag S, Apatay T, Guler MA, Gulgeç M. A surface crack in a graded coating subjected to sliding frictional contact. *Eng Frac Mech*. 2012;80:72-91.

20. Talezadehlari A, Nikbakht A, Sadighi M, Zucchelli A. Numerical analysis of frictional contact in the presence of a surface crack in a functionally graded coating substrate system. *Int J Mech Sci*. 2016;117:286-298.
21. Gu P, Asaro RJ. Cracks in functionally graded materials. *Int J Solids Struct*. 1997;34(1):1-17.
22. Jin ZH, Batra RC. R-curve and strength behavior of a functionally graded material. *Mater Sci Eng a*. 1998;242(1-2):70-76.
23. Dolbow JE, Gosz M. On the computation of mixed-mode stress intensity factors in functionally graded materials. *Int J Solids Struct*. 2002;39(9):2557-2574.
24. Dag S, Erdogan F. A surface crack in a graded medium under general loading conditions. *J Appl Mech*. 2002;69(5):580-588.
25. Dag S, Erdogan F. A surface crack in a graded medium loaded by a rigid stamp. *Eng Frac Mech*. 2002;69(14-16):1729-1751.
26. El-Borgi S, Abdelmoula R, Dag S, Lajnef N. A surface crack in a graded coating bonded to a homogenous substrate under general loading conditions. *J Mech Mater Struct*. 2007;2(7): 1331-1353.
27. Guo L-C, Wu L-Z, Zeng T, Ma L. Mode-I crack problem for a functionally graded orthotropic strip. *Eur J Mech a/Solids*. 2004;23(2):219-234.
28. Dag S, Ilhan KA. Mixed-mode fracture analysis of orthotropic functionally graded material coatings using analytical and computational methods. *J App Mech-Trans ASME*. 2008;75(5): 051104.
29. Dag S, Yildirim B, Sarikaya D. Mixed-mode fracture analysis of orthotropic functionally graded materials under mechanical and thermal loads. *Int J Solids Struct*. 2007;44(24):7816-7840.
30. Dag S. Thermal fracture analysis of orthotropic functionally graded materials using an equivalent domain integral approach. *Eng Frac Mech*. 2006;73(18):2802-2828.
31. Yildirim B. Investigation of thermal shock fracture in an edge-cracked functionally graded layer using finite element method. *J Fac Eng Arch Gazi Univ*. 2004;19(3):235-245.
32. Barber JR. Some thermoelastic contact problems involving frictional heating. *Q J Mech Appl Math*. 1976;29(1):1-13.
33. Hills DA, Barber JR. Steady motion of an insulating rigid flat-ended punch over thermally conducting half-plane. *Wear*. 1985;102(1-2):15-22.
34. Barber JR. Contact problems involving a cooled punch. *J Elasticity*. 1978;8(4):409-423.
35. Yevtushenko AA, Kulchytsky-Zhyhailo RD. Approximate solution of the thermoelastic contact problem with frictional heating in the general case of the profile shape. *J Mech Phys Solids*. 1996;44(2):243-250.
36. Kulchytsky-Zyhailo RD. A simplified solution for three-dimensional contact problem with heat generation. *Int J Eng Sci*. 2001;39(3):303-315.
37. Choi HJ, Paulino GH. Thermoelastic contact mechanics for a flat punch sliding over a graded coating/substrate system with frictional heating. *J Mech Phys Solids*. 2008;56(4):1673-1692.
38. Liu J, Ke L-L, Wang Y-S. Two-dimensional thermoelastic contact problem of functionally graded materials involving frictional heating. *Int J Solids Struct*. 2011;48(18):2536-2548.
39. Chen P, Chen S. Thermo-mechanical contact behavior of a finite graded layer under a sliding punch with heat generation. *Int J Solids Struct*. 2013;50(7-8):1108-1119.

40. Balci MN, Yildirim B, Dag S. Analysis of frictional contacts with heat generation considering temperature dependent properties. *Int J Mech Sci*. 2015;101-102:59-69.

41. Balci MN, Dag S, Yildirim B. Subsurface stresses in graded coatings subjected to frictional contact with heat generation. *J Thermal Stresses*. 2017;40(4):517-534.

42. ANSYS mechanical APDL theory reference. ANSYS Inc. 2016; release 17.1. Canonsburg PA, USA.

43. Yildirim B, Dag S, Erdogan F. Three dimensional fracture analysis of FGM coatings under thermomechanical loading. *Int J Fract*. 2005;132(4):371-397.

44. Simo JC, Laursen TA. An augmented Lagrangian treatment of contact problems involving friction. *Comput Struct*. 1992;42(1): 97-116.

45. Polat A, Kaya Y, Bendine K, Ozsahin TS. Frictionless contact problem for a functionally graded layer loaded through two rigid punches using finite element method. *J Mech des*. 2019; 35(5):591-600.

46. Yildirim B, Dag S, Erdogan F. Three dimensional fracture analysis of FGM coatings under thermomechanical loading. *Int J Fract*. 2005;132(4):371-397.

47. Lim IL, Johnston IW, Choi SK. Comparison between various displacement-based stress intensity factor computation techniques. *Int J Frac*. 1992;58(3):193-210.

48. Kim J-H, Paulino GH. Mixed-mode fracture of orthotropic functionally graded materials using finite elements and the modified crack closure method. *Eng Frac Mech*. 2002;69(14-16): 1557-1586.

49. Eischen JW. Fracture of non-homogenous materials. *Int J Fract*. 1987;34(1):3-22.

50. Jin ZH, Noda N. Crack tip singular fields in non-homogenous materials. *J Appl Mech*. 1994;61(3):738-740.

51. Kim J-H, Paulino GH. Finite element evaluation of mixed mode stress intensity factors in functionally graded materials. *Int J Numer Methods Eng*. 2002;53(8):1903-1935.

52. Fujimoto T, Noda N. Influence of the compositional profile of functionally graded materials on the crack path under thermal shock. *J am Ceram Soc*. 2001;84(7):1480-1486.

53. Toktaş S, Dag S. Oblique surface cracking and crack closure in an orthotropic medium under contact loading. *Theor Appl Fract Mec*. 2020;109:102729.